Springer

KSME

Journal of Mechanical Science and Technology 29 (12) (2015) 5477~5483
www.springerlink.com/content/1738-494x(Print)/1976-3824(Online)
DOI 10.1007/s12206-015-1149-z

Thermal analysis of high-speed permanent magnet motor with cooling flows supported on gas foil bearings: part II - bearing modeling and case studies †

Kyuho Sim[1], Yong-Bok Lee[2], Seok-Myeng Jang[3] and Tae Ho Kim[4,*]

[1]*Department of Mechanical System Design Engineering, Seoul National University of Science and Technology, Seoul, Korea*
[2]*Center for Urban Energy Systems, Korea Institute of Science and Technology, Seoul, Korea*
[3]*SEMS High-Tech. Engineering Co. Ltd, Daejeon, Korea*
[4]*School of Mechanical Systems Engineering, Kookmin University, Seoul, Korea*

(Manuscript Received March 23, 2015; Revised July 17, 2015; Accepted August 9, 2015)

Abstract

This paper presents the modeling of mechanical loss in Gas foil bearings (GFBs) that support a Permanent magnet (PM) motor. This paper also presents parametric studies to evaluate the effects of carrier harmonics in the input current and cooling-air supply on the motor thermal performance. Because GFB functions not only as a heat source but also as a thermal resistance, we model it as an equivalent element comprising a thermal conductor. The calculation of the bearing loss from the hydrodynamic analysis shows one-order-of-magnitude smaller values than the electromagnetic losses, thus indicating a slight effect on the PM motor performance. A case study shows the strong effects of the carrier harmonics and cooling-air supply on the motor thermal performance at a rotor speed of 35 krpm. A further study at an increased speed of 60 krpm shows significant increases in the motor losses and temperatures.

Keywords: Permanent magnet (PM) motor; Gas foil bearings (GFBs); Bearing loss; Electromagnetic losses; Input current carrier harmonics; Cooling; Thermal performance

1. Introduction

Permanent magnet (PM) electric motors and generators have been increasingly used in many applications such as in electric vehicles, wind power, micro gas turbines, and turbo compressors owing to their high efficiency, compactness, and high torque-to-inertia ratio [1-4]. The recent trend in PM machines toward high-speed operation and compact sizing demands high-speed bearings such as air-lubricated bearings with low friction and high-speed stability as well as accurate predictions of the thermal performance. Gas foil bearing (GFB) applications have been widespread in various high-speed and high-temperature rotating machinery owing to the enhanced rotor-dynamic performance of GFBs at high speeds and their capability of accommodating thermal deformations at high temperatures [5]. GFBs are a type of hydrodynamic gas/air bearing with a foil structure (a top foil and a bump foil) between a journal and a bearing housing. The hydrodynamic pressure in the air film supports the rotor weight and motion. Heshmat et al. [6] first conducted numerical hydrodynamic analyses of GFBs where each bump was modeled as a simple elastic foundation by solving the Reynolds equation for compressible flows. They showed that GFBs have higher static load capacity than plain journal bearings owing to their wider minimum film thickness. Peng and Carpino [7] conducted hydrodynamic analysis of GFBs to calculate the synchronous stiffness and damping coefficients using the finite element method and verified that Coulomb friction damping in the foil structure enhances the damping characteristics. In addition, GFBs have many other advantages such as low power loss, simple design, and light weight. Peng and Khonsari [8], San Andres and Kim [9], and Sim and Kim [10] developed thermal models of GFBs and analyzed their thermal performance. Their predictions showed that high rotor speed and static loading conditions increase the bearing temperatures, which significantly affects the static and dynamic performance of the bearing.

As a supplement work of Ref. [11], the present study aims to develop a thermal model of the GFBs to evaluate its effect on the PM motor performance and to conduct case studies to determine the effects of input current carrier harmonics, cooling flows, and rotor speed on the PM motor temperature.

2. Analyzed high-speed PM motor

The analyzed high-speed PM motor drives a two-stage turbo compressor whose shafts are coupled using a flexible

*Corresponding author. Tel.: +82 2 910 4723, Fax.: +82 2 910 4839
E-mail address: thk@kookmin.ac.kr
† Recommended by Editor Dongshin Shin

Table 1. Specifications of high-speed PM motor and its geometry and materials.

Motor design specification	Stator outer diameter	170	mm
	Stator inner diameter	73.5	mm
	Stack length	190	mm
	Number of s lots	36	
	Rotor diameter	69.5	mm
	Sleeve thickness	7.5	mm
	Number of poles	2	
	Air gap	2	mm
	PM diameter	19.75	mm
Coil specification	Phase	3	
	Turns per phase	12	
	Strand diameter	0.5	mm
	Number of strands	142	
	Fill factor	42.5	%
	Current density	7.75	A/mm^2
	Parallel branch	2	
Material properties	Stator core	35PN250	
	Shaft core	SCM440	
	Permanent magnet	Sm2Co24 (1.01T)	
	Rotor sleeve	Inconel 718	

* Turns per coil: 2; coil number: 6; rotor mass: 13.9 kg

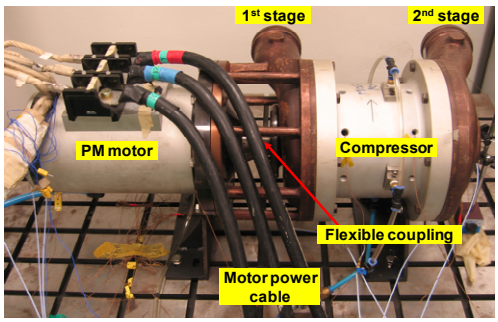

Fig. 1. Picture of a high-speed PM motor driving a two-stage turbo compressor via bellow flexible coupling.

coupling (see Fig. 1). The turbo compressor shaft has two impellers at its side ends and compresses air while rotating at the same speed as the motor. The diameters of the motor and compressor shafts at the bearing locations are 69.5 and 60.0 mm, respectively. The motor–compressor system is supported by four GFBs: two journal GFBs supporting radial rotor loads and one pair of thrust GFBs supporting axial loads. We note that Ref. [12] detailed the two-stage turbo compressor section. The PM motor was designed and developed with a rated power of 223 kW (voltage: 300 V; phase current: 570 A) at a maximum rotor speed of 60 krpm for the turbo compressor. Table 1 lists the specification of the analyzed PM motor and its detailed geometry and materials.

Fig. 2 shows the typical configuration of the bump-type test GFBs for the use in the high-speed PM motor: (a) journal GFB and (b) thrust GFB. The test GFBs are identical to those in Ref. [12]. The journal GFBs have an axial length of 60 mm and a radius of 35.75 mm. The thrust GFBs have six top-foil pads with an arc angle of 60° and inner and outer radii of 27 and 65 mm, respectively. The inclined plane angle at the leading edge, which generates the hydrodynamic film pressure in the air film, is 19.5°. Table 2 lists the geometry and materials

Table 2. Geometry and materials of the bump-type test GFBs, namely, journal and thrust, for the high-speed pm motor.

Journal GFB	Bearing radius	34.75 mm
	Bearing length	60.00 mm
	Bearing radial clearance	0.15 mm
	Top-foil thickness (MoS_2 coating, 0.02 mm)	0.22 mm
	Top-foil material	Inconel X-750
	Bump-foil thickness	0.20 mm
	Bump height	0.62 mm
	Bump pitch	5.66 mm
	Bump half-length	2.33 mm
	Bump-foil material	Stainless steel
Thrust GFB	Outer radius	65.00 mm
	Inner radius	27.00 mm
	Bearing axial clearance	0.15 mm
	Top-foil thickness (MoS_2 coating, 0.02 mm)	0.22 mm
	Top-foil material	Inconel X-750
	Number of top-foil pads	6
	Pad arc angle	60.0°
	Inclined part angle	19.5°
	Bump-foil thickness	0.20 mm
	Bump height	0.50 mm
	Bump pitch	5.00 mm
	Bump half-length	1.30 mm
	Bump-foil material	Stainless steel

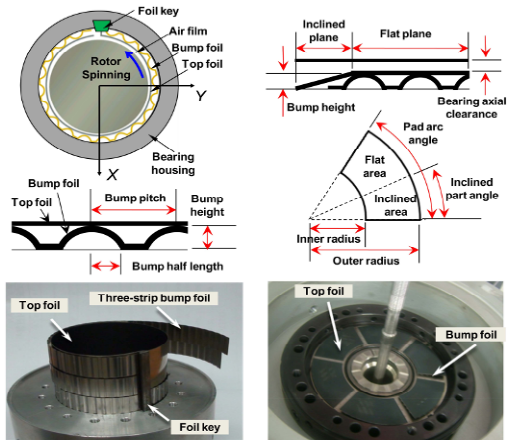

(a) (b)

Fig. 2. Configuration of bump-type test GFBs for high-speed PM motor: (a) journal GFB; (b) thrust GFB.

Table 3. Geometry of the Axial Cooling Fan Installed at the Rotor left end.

Blade number	7	
Blade height (H_B)	5	mm
Tip clearance (C_B)	1	mm
Blade inlet angle ($\phi_{B,in}$)	52	Degree
Blade exit angle ($\phi_{B,out}$)	73	Degree
Blade axial length (L_B)	29.8	mm

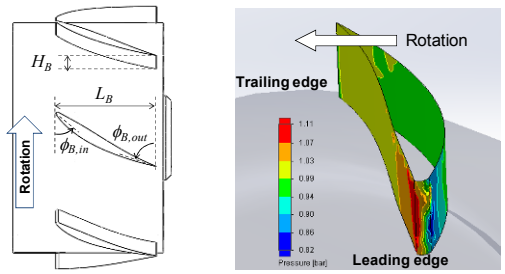

(a) (b)

Fig. 3. Preliminary flow simulation of the axial cooling fan at a rotor speed of 35 krpm: (a) schematic view; (b) predicted pressure distribution on the fan blade.

of the bump-type test GFBs, i.e., journal, and thrust, for the high-speed PM motor.

3. Losses and thermal models of GFBs

3.1 Hydrodynamic analysis of GFBs

The analyses of the journal and thrust GFBs use the computational models in Refs. [13, 14], respectively. The Reynolds equation, derived from the continuity and Navier–Stokes equations, describes the gas pressure within the film thickness between the rotor and bearing surface. The models assume isothermal and isoviscous ideal gas properties to solve the gas-film pressure field and a two-dimensional flat shell supported on axially distributed linear springs to analyze the top- and bump-foil structures. Non-slip-flow boundary conditions between the gas flow and the rotor/bearing surfaces and non-tilt motions of the rotor are assumed to simplify the GFB models [14]. Once the hydrodynamic analyses of the GFBs have calculated the rotor equilibrium position and the corresponding pressure distribution in the air film, the pressure gradient and rotor angular speed determine the bearing torque and power loss.

3.2 Mechanical loss and thermal model of GFBs

The mechanical bearing losses are calculated at an equilibrium position, where the rotor weight balances the vertical reaction forces from the hydrodynamic pressure of the journal GFBs and the axial force due to the cooling fan balances the axial reaction forces from the thrust GFB. The aerodynamic forces from the two impellers installed at both ends of the compressor rotor are assumed to balance each other, i.e., the net force can be ignored. The total rotor weight of 136 N is distributed as 74.5 and 61.5 N on the left and right GFBs, respectively. The axial cooling fan [Fig. 3(a)] installed at the left end of the rotor generates an axial force of 6.6 N toward the left direction, as shown in Fig. 1. The axial force is calculated from flow simulations. Fig. 3(b) shows the predicted pressure distribution on the cooling fan blade at a rotor speed of 35 krpm, where the left blade surface in the rotating direction shows higher pressure than the opposite surface. Table 3 lists the geometry of the axial cooling fan.

Table 4. Mechanical losses of the Journal and Thrust GFBs at rotor speed of 35 kRPM predicted from the hydrodynamic analyses.

GFBs		Bearing loss (W)
Thrust GFB	Left	110.5
	Right	20.2
Journal GFB	Left	50.1
	Right	41.3

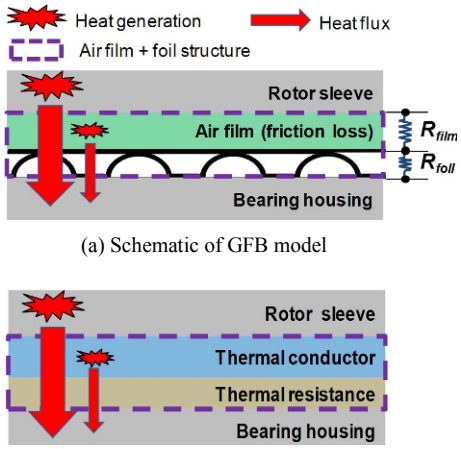

(a) Schematic of GFB model

(b) Equivalent theermal model of GFB

Fig. 4. Thermal model of the GFBs considering bearing loss in the air film and thermal resistance of air and foil structures: (a) schematic of GFB model; (b) equivalent thermal model of GFB.

Table 4 lists the predicted bearing losses of the journal and thrust GFBs at a rotor speed of 35 krpm from the hydrodynamic analyses. The mechanical loss of the left thrust GFB with an axial load is much higher than that of the right GFB because of its small bearing-film thickness. The mechanical loss of the left journal GFB, which supports a heavier load, is slightly higher than that of the right GFB. We note that the thrust collar is located near the left journal GFB. The total mechanical bearing loss is 222 W.

The GFB with an air film and a foil structure acts not only as a heat source (shear friction loss in the air film between the rotor and the top foil) in the thermal model of the high-speed PM motor but also as a thermal resistance that separates the thermal fields of the rotor and motor casing to some extent. As a thermal component of the motor, each GFB is modeled as an equivalent element comprising a thermal conductor with a heat source and a thermal resistance, as shown in Fig. 4. The

heat source assumes the predicted bearing losses listed in Table 5. The thermal resistances of the air film and the top and bump foils are connected in series. The thermal resistance R_{eq} of the equivalent GFB element is estimated from the equation $R_{eq} = R_{film} + R_{foil}$, yielding $R_{eq} = 5.6 \times 10^{-3}$ m·K/W. Thermal resistance is defined as $R = t/k$, where t is the foil-structure or air-film thickness and k is the corresponding thermal conductivity. The thermal conductivity of the bump foil (Inconel X-750) and that of the air film are 15 and 0.028 W/(m·K), respectively. The thicknesses of the foil structure and the air film are 0.82 and 0.1 mm, respectively. The net thermal conductivity of the top- and bump-foil layers is 2% of that of the foil material because of the smaller effective bump-foil area and the thermal contacts on the bump interfaces to the mating surfaces (the effective bump cross-sectional area is 7.7% of the bump pitch and thickness, and the assumed thermal conductivity of the contact interfaces is 25%). Details of the thermal model of the GFBs, particularly those related to the film-thickness estimation and thermal contact phenomenon, are provided in Ref. [10].

At high temperature, the mechanical loss in GFBs can also increase due to the decrease in the bearing clearance and increase in the air viscosity [15]. In a typical rotor-GFB system, the increase in the rotor temperature is higher than that in the bearing-housing temperature because heat sinks are normally connected structurally to the bearing housing. However, the bearing losses listed in Table 4 are found to be one order of magnitude smaller than the electromagnetic losses (see Table 2 in Ref [11]). Therefore, the temperature effect on the bearing loss is presently neglected. More details on the thermal behavior of the rotor-GFB systems at high temperature are presented in Refs. [10, 16].

4. Case studies

On the basis of the validated thermal model of the high-speed PM motor (reference model), two case studies are conducted to investigate the thermal effects of carrier harmonics included in the motor input current and the cooling air supplied by the axial fan at the rotor end. In the first case study, a sine-wave input current where the carrier harmonics are removed (Fig. 2(a) in Ref. [11]) is applied to the reference thermal model with cooling flow. For the second case study, no cooling air from the fan blades in Fig. 3 is assumed to flow to the reference model with the measured input current. Iterative solutions are also obtained between the temperature and electromagnetic losses.

Table 5 lists the summary of the calibrated electromagnetic losses, temperatures of the corresponding part, and motor temperatures of the high-speed PM motor at a rotor speed of 35 krpm for the case study with a sine-wave input current and that with no cooling-air supply compared with the reference model. The cooling-air and water inlet temperatures are 31 and 15°C, respectively, which are identical to those in the reference model. The electromagnetic losses are calibrated at predicted temperatures of the related parts in Ref. [11]. The stator core loss is calibrated with an increase of 78% from that of the predicted sine-wave current (Table 3 in Ref. [11]).

Symbols (+) and (-) denote the increase and decrease, respectively, of the losses or temperatures from the reference model. For the first case, i.e., with the sine-wave input current, the calibrated stator and rotor losses are greatly reduced by

Table 5. Calibrated electromagnetic losses, related part temperatures, and motor temperatures of the high-speed PM motor at rotor speed of 35 kRPM for two case studies and the reference model.

		Reference model (Measured input current with cooling flows)	Sine-wave Input current (with cooling flows)		Measured Input current (no cooling-air supply)	
Electro-magnetic loss (W)	Stator loss	2138	999	-53.3%	2138	+0.0%
	Rotor loss	1075	142	-86.8%	1118	+4.0%
	Copper loss	515	474	-8.0%	547	+6.2%
Related part temperature (°C)	Stator core	76.5	50.6	-33.9%	95.4	+24.7%
	Rotor sleeve	125.8	59	-53.1%	169.7	+34.9%
	Coil	78.8	54.2	-31.2%	98.3	+24.7%
Motor temperature (°C)	Rotor	113.7	56.9	-50.0%	150.5	+32.4%
	Stator	62.6	42.8	-31.6%	76.9	+22.8%
	Left exit (air)	43.4	39.5	-9.0%	-	-
	Right exit (air)	51.9	46	-11.4%	-	-
	Exit (water)	24.4	21.7	-11.1%	28.3	+16.0%

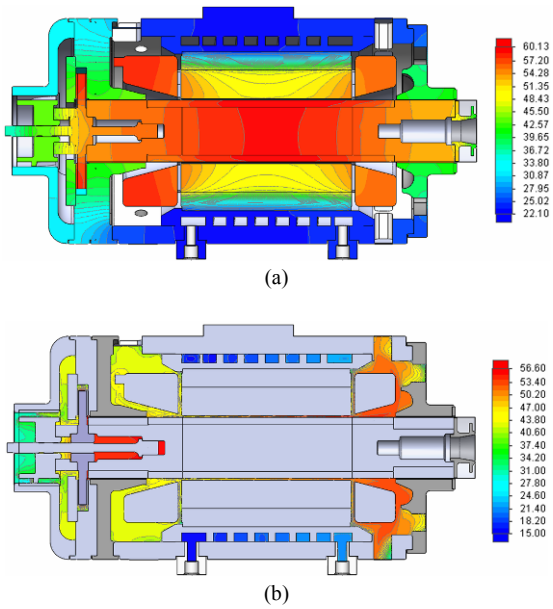

Fig. 5. Temperature distributions: (a) in a solid structure; (b) of the cooling flows in the high-speed PM motor at a rotor speed of 35 krpm for a sine-wave current input.

53% and 89%, respectively. As a result, the rotor and stator temperatures in the reference model are also greatly reduced by 34% and 53%, respectively, thus implying large temperature increases due to the carrier harmonic components in the motor input current. Note that the temperature decreases in the rotor due to the dramatic removal of the carrier harmonics. The cooling flow temperatures are also reduced due to the decreased temperature in the motor. For the second case with no cooling-air supply, the calibrated electromagnetic losses show virtually negligible changes compared with those of the reference model. However, the removal of the cooling-air flow results in a large increase in the temperature of the rotor and stator by ~32% and ~23%, respectively, compared with those of the reference model. Normally, water cooling is believed to be dominant for heat removal in the PM motor; however, the simulation results demonstrate that the cooling-air flow is also important, especially in the rotor. The removal of the fan blades also decreases the thrust bearing loss; however, the effect is minimal because the bearing loss is much smaller than the electromagnetic losses. The case studies show that both the removal of the carrier harmonics and the air-cooling supply decrease the temperature in the rotor more than that in the stator. Note that the rotor is "thermally floating" without strong heat sinks. In practice, maintaining the rotor temperature steady and low is very important from the viewpoint of rotor dynamics and lubrication in high-speed rotating machines. In worst cases, excessive thermal expansions caused by elevated rotor temperature can cause rotor-bearing system failure due to thermal seizures.

Fig. 5 shows the temperature distribution (a) in a solid structure and (b) of the cooling flows in a high-speed PM motor at a rotor speed of 35 krpm for a sine-wave current input. Fig. 6 shows the temperature distribution (a) in a solid structure and (b) of the cooling flows in a high-speed PM motor at a rotor speed of 35 krpm without cooling air. Note that only small changes in the flow pressure and velocity of the cooling flows are observed; hence, they are omitted for simplicity.

A further study is conducted with the reference model using the measured input current on a PM motor that drives a turbo compressor at a rotor speed of 60 krpm (see Appendix for the measured current and loss analysis). The cooling-air and water inlet temperatures are 31 and 15°C, respectively, which are identical to those in the reference model. Iterative solutions are also achieved between the temperature and electromagnetic losses. The electromagnetic losses are calibrated at predicted temperatures of the related parts, similar to those in Ref. [11].

Table 6 lists the comparison of the electromagnetic losses and motor temperatures of the high-speed PM motor of the reference model at 35 krpm and those of the case study model at 60 krpm. The result shows remarkable increases in the electromagnetic losses by 76% compared with the reference model at a rotor speed of 35 krpm, which result from the highly increased motor input power with significant carrier harmonics to drive the high-load turbo compressor. As a result, the motor temperatures also greatly increase by 50% com-

Table 6. Electromagnetic losses and motor temperatures of the high-speed PM motor at 35 and 60 kRPM.

Loss (watt)	Reference model (35 krpm)	High speed model (60 krpm)	Percentage difference (%)
Stator loss	2,138	3,165	+48.0%
Rotor loss	1,075	2,060	+91.6%
Copper loss	515	1,330	+158.3%
Temperature(°C)			
Coil	79	118	+49.4%
Stator core	77	116	+50.6%
Rotor	114	176	+54.4%
Cooling-air exit	48	69	+43.8%
Cooling-water exit	24	34	+41.7%

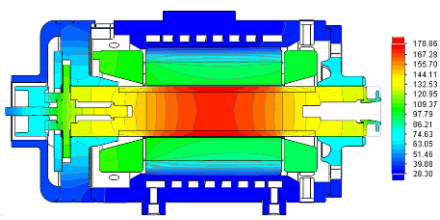

(a)

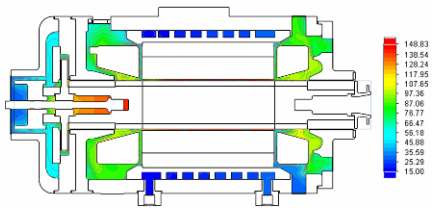

(b)

Fig. 6. Temperature distributions: (a) in a solid structure; (b) of the cooling flows in the high-speed PM motor at a rotor speed of 35 krpm with no cooling air.

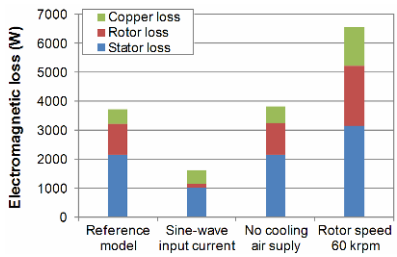

(a)

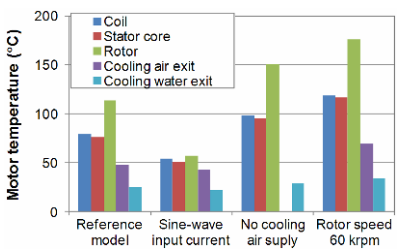

(b)

Fig. 7. (a) Electromagnetic losses; (b) predicted motor temperatures of the high-speed PM motor of the reference model and the three case study models.

pared with the reference model. In particular, the coil temperature approaches 120°C. When we recall that the coil temperature is an average value of all the coil temperatures and the prediction underestimates by ~10% [11], the actual maximum coil temperature is much higher than the predicted average temperature, which is likely to result in a thermal problem in the coil. Fig. 7 shows the summary of the case studies listed in Tables 5 and 6, namely, (a) calibrated electromagnetic losses and (b) predicted motor temperatures of the high-speed PM motor at rotor speeds of 35 krpm for the reference model, sine-wave input current model, and model with no supply of cooling air and those at 60 krpm for the high-speed model.

5. Conclusion

This paper has presented the loss calculation of GFBs that support a PM motor and the effects of the input current carrier harmonics, cooling flows, and rotor speed on the motor temperature. The model predictions show that the power loss of the GFBs predicted from the hydrodynamic analysis is ~222 W, which is an order of magnitude smaller than the electromagnetic losses calculated in Ref. [11]. Therefore, it appears that the mechanical losses due to the GFBs are negligible. Case studies conducted based on the established thermal model show that the removal of the input current carrier harmonics (or using only a sine-wave input current) considerably decreases the electromagnetic losses and the motor temperature, i.e., by a maximum of 86.8 % (rotor loss) and 53.1 % (rotor sleeve), respectively, compared with the results of the reference model in Ref. [11]. The removal of the cooling-air supply slightly increases the electromagnetic losses, i.e., by a maximum of 6.2 % (copper loss), and the motor-part temperature to some degree, i.e., by a maximum of 34.9 % (rotor sleeve). The other case study on the increase in the rotor speed to 60 krpm reveals significant increases in the electromagnetic losses by a maximum of 158.3% (copper loss) and the motor temperature by a maximum of 54.4% (rotor). The present study can serve as a benchmark for effective thermal design of high-speed PM motor.

Acknowledgement

This material is based upon the works supported by Korea Institute of Science and Technology (KIST) Research Project: Development of Fundamental Energy Conversion Technologies for Efficient Electricity Consumption in Metropolis. The authors also acknowledge the support by the Human Resources Development Program (No.20134040200580) of the Korea Institute of Energy Technology Evaluation and Planning (KETEP) funded by the Ministry of Knowledge Economy, Republic of Korea.

References

[1] R. T. Doucette and M. D. McCulloch, Modeling the prospects of plug-in hybrid electric vehicles to reduce CO_2 emissions, *Appl. Energy,* 88 (7) (2011) 2315-2323.

[2] Y. Y. Hsu and S. Y. Lu, Design and implementation of a hybrid electric motorcycle management system, *Appl. Energy,* 87 (11) (2010) 3546-3551.

[3] S. Eriksson and H. Bernhoff, Loss evaluation and design optimization for direct driven permanent magnet synchronous generators for wind power, *Appl. Energy,* 88 (1) (2011) 265-271.

[4] M. Moya, J. C. Bruno, P. Eguia, E. Torres, I. Zamora and A. coronas, performance analysis of a trigeneration system based on a micro gas turbine and an air-cooled, indirect fired, ammonia–water absorption chiller, *Appl. Energy,* 88 (12) (2011) 4424-4440.

[5] S. Howard, Misalignment in gas foil journal bearings: an experimental study, *ASME J. Eng. Gas Turbines Power,* 131 (2) (2009) 022501.

[6] H. Heshmat, J. A. Walowit and O. Pinkus, Analysis of gas-lubricated foil journal bearings, *ASME J. Lubr. Technol.,* 105 (4) (1983) 647-655.

[7] J. P. Peng and M. Carpino, Coulomb friction damping effects in elastically supported gas foil bearings, *STLE Tribol. Trans.,* 37 (1) (1994) 91-98.

[8] Z.-C. Peng and M. M. Khonsari, A thermohydrodynamic analysis of foil journal bearings, *ASME J. Tribol.,* 128 (2006) 534-540.

[9] L. San Andrés and T. H. Kim, Thermohydrodynamic analysis of bump type gas foil bearings: a model anchored to test data, *ASME J. Eng. Gas Turbines Power,* 132 (4) (2010) 042504.

[10] K. Sim and T. H. Kim, Thermohydrodynamic analysis of bump-type gas foil bearings using bump thermal contact and inlet flow mixing models, *Tribol. Intl.,* 48 (2012) 137-148.

[11] K. Sim S.-M. Jang, Y.-B. Lee and T. H. Kim, Thermal analysis of high speed permanent magnet motor supported on gas foil bearings: Part I – Coupled thermal and loss modeling, Submitted to *J. Mech. Sci. Technol.* (2015).

[12] Y. B. Lee, S. B. Cho, T. Y. Kim, C. H. Kim and T. H. Kim, Rotordynamic performance measurement of an oil-free turbocompressor supported on gas foil bearings, *Proc. IFToMM Int. Conf. on Rotordynamics*, Seoul, Korea (2010) 420-426.

[13] L. S. Andrés and T. H. Kim, Analysis of gas foil bearings integrating fe top foil models, *Tribol. Intl*., 42 (1) (2009) 111-120.

[14] D.-J. Park, C.-H. Kim, G.-H. Jang and Y.-B. Lee, Theoretical considerations of static and dynamic characteristics of air foil thrust bearing with tilt and slip flow, *Tribol. Intl*., 41 (2008) 282-295.

[15] M. Salei, E. Swanson and H. Heshmat, Thermal features of compliant foil bearings —theory and experiments, *ASME J. Tribol*., 123 (3) (2001) 566-571.

[16] T. H. Kim, J. W. Song, Y. B. Lee and K. Sim, Thermal performance measurement of a bump type gas foil bearing floating on a hollow shaft for increasing rotating speed and static load, *ASME J. Eng. Gas Turbines Power*, 134 (2) (2012) 024501.

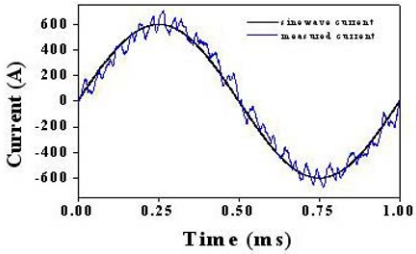

(a)

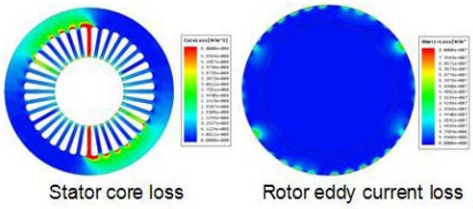

(b)

Fig. A.1. (a) Measured phase current in the high-speed PM motor driving a turbo compressor at a rotor speed of 60 krpm; (b) predicted stator core loss and rotor eddy current loss.

Appendix

Fig. A.1(a) shows the measured phase current in the high-speed PM motor driving a turbo compressor at a rotor speed of 60 krpm, and Fig. A.1(b) shows the predicted stator core loss and rotor eddy-current loss. The electromagnetic loss analyses were conducted using the measured phase current. Incidentally, the mechanical losses were 325 and 220 W for the thrust and journal GFBs, respectively.

Kyuho Sim received the M.S. degree in mechanical engineering from KAIST, Daejon, Korea, in 2002 and Ph.D. degree in mechanical engineering from Texas A&M University, College Station, TX, in 2007. He joined Samsung Advanced Institute of Technology, Suwon, Korea, in 2007, and Korea Institute of Science and Technology, Seoul, Korea, in 2010. In 2013, he joined the Department of Mechanical System Design Engineering at Seoul National University of Science and Technology as an assistant professor. His research interests are lying on sustainable, efficient energy conversion and harvesting systems such as micro turbine generators, Stirling engine generators, vibro wave convertors, etc.

Yong-Bok Lee, KIST, Principal researcher and Professor, received his Ph.D. (1997) degrees in Mechanical Engineering for the Hanyang University. He charged head of energy mechanics center in KIST from 2007 to 2011. And he is a professor of UST. His main research topic is a hydrodynamic bearing and its application from the beginning of 1990. Dr. Lee's current research issues are controllable tribo-elements such as a hybrid bearing (HFMB; Air foil bearing and Active magnetic bearing) and ball bearings operated cryogenic condition for turbo pump of LRE (liquid rocket engine).

Seok-Myeong Jang received the B.S., M.S., and Ph.D. degrees in electrical engineering from Hanyang University, Seoul, Korea, in 1976, 1978, and 1986, respectively. He joined Chungnam National University, Daejeon, Korea, in 1978-2014. Currently he is an Emeritus Professor and a CEO of SEMS High-tech Engineering. His research interests include Special Electric Machines (SEMS) design and analysis for high-speed motor/generator system, magnetic levitation vehicle, and renewable energy system, such as wind power generator and flywheel energy storage.

Tae Ho Kim received the B.S. and M.S. degrees in mechanical engineering from Hanyang University, Seoul, Korea, in 2000 and 2002, respectively, and the Ph.D. degree in mechanical engineering from Texas A&M University, College Station, TX, in 2007. In 2009, he joined Korea Institute of Science and Technology, Seoul, Korea, and worked on the development of oil-free rotating systems with high power density. In 2012, he joined the School of Mechanical Systems Engineering, Kookmin University as an assistant professor. His main research fields are gas/fluid film bearing analysis and performance identification, and structural/rotor dynamics in micro/macro turbomachinery systems.